

## Stability and electronic properties of edges of $\text{SnS}_2$

Tao Yan<sup>1,\*</sup>, Pratap M. Rao,<sup>2</sup> and N. Aaron Deskins<sup>1,3</sup>

<sup>1</sup>*Materials Science and Engineering program, Worcester Polytechnic Institute, Worcester, Massachusetts 01609, USA*

<sup>2</sup>*Department of Mechanical Engineering, Worcester Polytechnic Institute, Worcester, Massachusetts 01609, USA*

<sup>3</sup>*Department of Chemical Engineering, Worcester Polytechnic Institute, Worcester, Massachusetts 01609, USA*



(Received 2 April 2020; revised 29 July 2020; accepted 23 September 2020; published 22 October 2020)

Because of its two-dimensional structure and semiconducting properties, tin disulfide ( $\text{SnS}_2$ ) is of interest for many applications, such as photocatalysis, photovoltaics, sensing, and electronics. While the atomic and electronic structure of bulk and monolayer  $\text{SnS}_2$  have been studied, much less is known about the edges of layers. Such edges could have a major influence on the performance of  $\text{SnS}_2$ . This paper reports on density functional theory (DFT) simulations of the atomic and electronic structure of the edges of  $\text{SnS}_2$ . We modeled several different edge terminations at various S coverages and orientations, as well as performed thermodynamic analysis of edge terminations. Our results show that edges with 0% and 50% S atoms are most stable and that higher S coverage are unstable. We directly link edge stability with environmental temperature and pressure, which will guide the experimental synthesis of  $\text{SnS}_2$  materials. We found all the edges to be semiconducting, unlike other metal chalcogenides, and that the band gap energy decreased with increasing S coverage. Semiconducting edges could lead to lower charge recombination rates and better photocatalytic performance. Our calculations also show that edges may have direct or indirect band gaps, depending on the edge termination. Finally, we examined the reactivity of edges through hydrogen dissociation and found edges to be more reactive than basal planes. Our work provides important details on the nature of  $\text{SnS}_2$  edges and how these edges influence the electrical and chemical features of  $\text{SnS}_2$ .

DOI: [10.1103/PhysRevB.102.155306](https://doi.org/10.1103/PhysRevB.102.155306)

### I. INTRODUCTION

Two dimensional (2D) materials have been studied for years because of their unique mechanical, chemical and optical properties [1–3]. One of the earliest 2D materials to be studied was graphene [4], but many more 2D materials have been discovered and studied, including layered metal dichalcogenides (LMDs), for instance,  $\text{MoS}_2$  [5–8],  $\text{WSe}_2$  [9,10],  $\text{WS}_2$  [11,12], and  $\text{NbS}_2$  [13]. Tin disulfide ( $\text{SnS}_2$ ) is an LMD that has attracted interest because it is cheap, composed of abundant, nontoxic elements, and has interesting properties.

$\text{SnS}_2$  is promising for a number of applications, including photoelectrochemical catalysis [14,15], electrochemical catalysis [16], photoconductors [17,18], photovoltaics [19,20], lithium ion batteries [21,22], field-effect transistors (FETs) [23], and sensors [24,25].  $\text{SnS}_2$  can be exfoliated to very thin layers and has been used as ultrathin and flexible FETs. It has also been used as the electron transport layer (ETL) in perovskite solar cells [19,23] because of its layered structure and high carrier mobility. Moreover, the multilayered structure also helps  $\text{SnS}_2$  have large accessible volume to store Li, and Li can be released and stored between layers readily [22]. As a semiconducting material with a 2.1 to 2.4 eV band gap energy,  $\text{SnS}_2$  can absorb visible light, and therefore has been studied for photovoltaic and photodetector applications

[18–20]. Similar to other LMDs, such as  $\text{MoS}_2$ ,  $\text{SnS}_2$  has also been used in photoelectrocatalysis [14,15]. For instance,  $\text{SnS}_2$  was studied for water splitting [26] because the conduction and valence bands of  $\text{SnS}_2$  straddle the oxidation and reduction potentials of water, which gives favorable alignment for water splitting.

A similar 2D material is 2H- $\text{MoS}_2$ , which has several interesting properties. One well known property of 2H- $\text{MoS}_2$  is that monolayer  $\text{MoS}_2$  has a direct band gap [27], while bulk 2H- $\text{MoS}_2$  has an indirect band gap. This makes monolayer 2H- $\text{MoS}_2$  more efficient for light absorption and emission. On the other hand, the metallic nature of 2H- $\text{MoS}_2$  flake edges, as discovered through density functional theory (DFT) simulations and high-resolution scanning tunneling microscopy (STM) [28,29], leads to the edges being recombination sites for photo-excited charges. Metallic edges are also not ideal for transistors and sensors because these can cause short circuit paths across the metallic electrodes, resulting in low current on/off ratios and high power consumption. The edge configurations and electronic structure of 2H  $\text{MoS}_2$  have been well-documented [30,31] through experiment and theory. Similar details for  $\text{SnS}_2$  are missing in the literature.

Edges are important to the performance and properties of  $\text{SnS}_2$  as well. Edges and defects of  $\text{SnS}_2$  nanoflakes were shown to improve photoelectrochemical performance [15,32]. Edges may also occur when incomplete growth of  $\text{SnS}_2$  occurs, such as in missing regions of a basal plane, or in harsh environments that deteriorate the layers [15]. In previous experimental work [15], we showed that edges are

\*tyan@wpi.edu

electrochemically active, but the atomic and electronic nature of such  $\text{SnS}_2$  edges are unclear. Better understanding of the edges is needed in order to tailor effective nanostructures for targeted applications.

There exist several density functional theory (DFT) studies of  $\text{SnS}_2$ , which provide quantum mechanical modeling results. These include the study of the properties of monolayer, multilayers, and/or bulk [33,34], the effect of van der Waals interactions [35], doping of  $\text{SnS}_2$  [36,37], defects [38,39], heterostructures [40], and others. Edges have been modeled in  $\text{SnS}_2$  nanoribbons [41–43]. Such studies provide important details on  $\text{SnS}_2$  edge sites, but focus on novel structures that may not be readily present or synthesized in experimentally relevant samples. Chia *et al.* [44] modeled hydrogen adsorption to  $\text{SnS}_2$  edges but did not provide detailed information about the electronic and structural properties of such edges.

The structure and electronic properties of  $\text{SnS}_2$  edges are not fully understood, which limits the applicability of  $\text{SnS}_2$  in many applications. This paper aims to model  $\text{SnS}_2$  edges using DFT. The stability of both multilayer and monolayer  $\text{SnS}_2$  edges with different S terminations have been modeled. Electronic properties of various edges were also determined, which links edge structure to electronic behavior. Our work is the first of its kind to characterize  $\text{SnS}_2$  edges in such a manner at the atomic-scale using DFT.

## II. COMPUTATIONAL METHODS

### A. DFT simulation details

All simulations utilized DFT with the Vienna *ab initio* simulation package (VASP) [45–48]. The electronic and ionic relaxations convergence criteria were  $10^{-5}$  and  $0.01$  eV/Å, respectively. A plane wave cutoff energy of  $400$  eV was used. A  $6 \times 6 \times 2$  Gamma centered  $k$ -point grid was used for modeling bulk and monolayer  $\text{SnS}_2$ . A single  $k$  point was used for calculations of multilayer edges and monolayer edges, since these calculations involve larger supercells. The generalized gradient approximation (GGA) with the Perdew-Burke-Ernzerhof (PBE) [49] exchange correlation functional was used for all geometry optimizations. We employed the Heyd-Scuseia-Ernzerhof (HSE06) hybrid exchange correlation functional [50] for calculating density of states (DOS). However, using HSE06 required such large computational time for band structure calculations, so we calculated the band structure of multilayer and monolayer edges with the PBE functional, which gave very similar results to HSE06 (Fig. S1 [51]). The choice of points in reciprocal space for band structure calculations were guided using the SEEK-PATH program [52]. Grimme's zero damping DFT-D3 approach [53,54] was used in all calculations to include van der Waals forces, which are important for inter-layer interactions.

$\text{SnS}_2$  has two main crystal structures:  $2\text{H}(\bar{P}\bar{3}m1)$  and  $4\text{H}(P6_3mc)$ . The  $2\text{H}$  phase is the most stable structure, and therefore is the most common phase studied [24,26]. We modeled this phase in our work. Each layer of  $2\text{H-SnS}_2$  was identical, where a row of Sn atoms is sandwiched between two A-B stacked S layers. These S-Sn-S layers stack on top of each other, attracted to each other by van der Waals interactions, similar to other 2D materials.

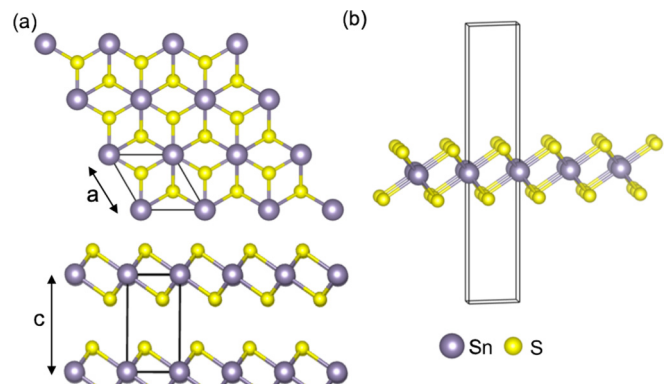


FIG. 1. The simulation cells used for modeling bulk and monolayer  $\text{SnS}_2$ . Purple balls represent Sn atoms and the yellow balls are S atoms. (a) The top and side views of bulk  $\text{SnS}_2$ . The solid lines indicate the unit cell. (b) The side view of a unit cell of monolayer  $\text{SnS}_2$ .

In this work, we modeled two types of structures:  $\text{SnS}_2$  layers with no edges and  $\text{SnS}_2$  with edges.  $\text{SnS}_2$  layers with no edges are essentially infinite sheets. Bulk  $\text{SnS}_2$  consists of these sheets stacked continually next to each other, while monolayer  $\text{SnS}_2$  consists of a single sheet. Figure 1 depicts the cells we used to model layered  $\text{SnS}_2$  structures (no edges). We also modeled  $\text{SnS}_2$  sheets that had edges cut from them. These structures resembled ribbons, being infinitely long in the  $x$  direction, and having finite thickness in the  $z$  direction. Figure 2 depicts these structures, along with the exposed edges. The (1010) facet is the most stable termination observed in previous experiments [15,55], so was used in the simulations. For the ribbon models, the ribbons were eight Sn layers thick. These ribbons were chosen so that the middle two layers behaved as bulk  $\text{SnS}_2$ , while the top and the bottom layers were edges. To validate that this ribbon width was sufficient, we calculated the DOS for monolayer ribbons being eight and ten Sn layers thick, as shown in Fig. S2 [51]. The DOS are nearly identical, indicating that an eight-layer ribbon is sufficiently wide. We also tested the  $k$ -point mesh by comparing DOS for a monolayer ribbon using  $1 \times 1 \times 1$  and  $2 \times 2 \times 1$   $k$ -point meshes. The DOS (Fig. S3 [51]) were nearly identical, indicating that a single  $k$  point is sufficient for describing the ribbons. There was  $\approx 18$  Å vacuum in the  $z$  direction between ribbons. We modeled both the top and bottom edges of the ribbons with identical terminations. Figure 2 shows the multilayer edges having no S atoms terminating the edges (0% S coverage). More S atoms could be added to the edges, resulting in higher S coverage. We modeled different S coverages by adding S atoms to these edges. For the monolayer ribbon, the  $\text{SnS}_2$  single layer is separated from other single layers by a distance of  $14$  Å, so that the interactions between two layers can be ignored.

### B. Stability of different edges

A primary goal of our work was to determine the atomic arrangement/configurations for the  $\text{SnS}_2$  edges, as well as their stability. To determine the most stable edges of  $\text{SnS}_2$  under various environmental conditions, we calculated edge

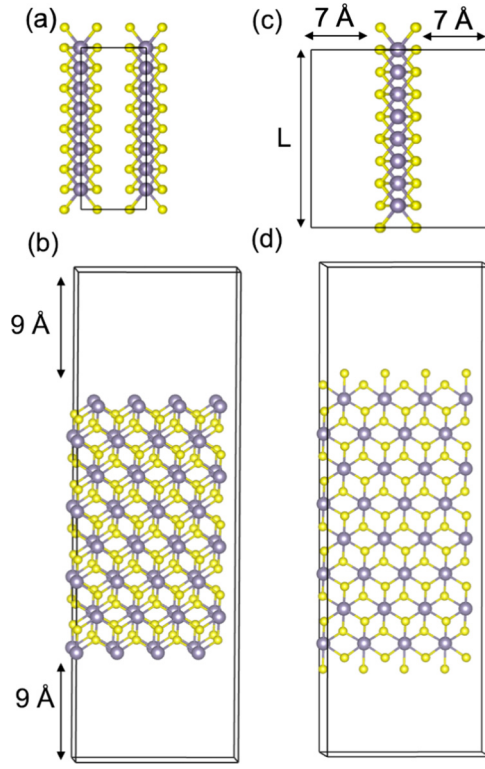


FIG. 2. The simulation cells used for modeling edges of  $\text{SnS}_2$ . The structures consist of ribbons with exposed edges on the top and bottom of the ribbons. Purple balls represent Sn atoms and the yellow balls are S atoms. (a) The top view of the cell with multilayer  $\text{SnS}_2$  ribbons. The solid lines indicate the unit cell. (b) The side view of the cell with multilayer  $\text{SnS}_2$  ribbons. The exposed edges are separated from each other by  $\approx 18 \text{ \AA}$ . (c) The top view of the cell with a single  $\text{SnS}_2$  ribbon (monolayer). The ribbons are separated from each other by  $\approx 14 \text{ \AA}$ . (d) The side view of the cell with a single  $\text{SnS}_2$  ribbon. The length of the ribbons in the cell are shown by the variable  $L$ .

formation energies using DFT results of the multilayer and monolayer ribbons (Fig. 2). We used the approach found in previous work to calculate surface formation energies [56–59]. The surface (or edge) formation energy,  $\gamma$ , of the multilayer ribbon can be determined by the formula typically used for slabs:

$$\gamma_{\text{multilayer ribbon}} = \frac{(G_{\text{ribbon}}^i - N_{\text{Sn}}\mu_{\text{Sn}} - N_{\text{S}}\mu_{\text{S}})}{2A}. \quad (1)$$

$A$  is the area of the surface.  $N_{\text{Sn}}$  and  $N_{\text{S}}$  are the number of Sn and S atoms in the ribbons.  $\mu_{\text{Sn}}$  and  $\mu_{\text{S}}$  are the chemical potentials of Sn and S. The  $A$  value for the multilayer ribbon structure was taken from the cell lattices parallel to the surface, or the  $x$  length multiplied by the  $y$  length shown in Fig. 2(a). The area of the multilayer ribbons follows conventional work with slabs since the exposed surface all fits within the simulation cell. In the case of a monolayer ribbon [Figs 2(c) and 2(d)], defining a surface area is not straightforward. The area of the exposed surface is not fully clear. Rather, we normalize the formation energy of this ribbon in

terms of length  $L$ :

$$\gamma_{\text{monolayer ribbon}} = \frac{(G_{\text{ribbon}}^i - N_{\text{Sn}}\mu_{\text{Sn}} - N_{\text{S}}\mu_{\text{S}})}{2L}. \quad (2)$$

The chemical potentials of Sn and S can be written in terms of the bulk  $\text{SnS}_2$  chemical potential,  $\mu_{\text{SnS}_2}$ :

$$\mu_{\text{SnS}_2} = \mu_{\text{Sn}} + 2\mu_{\text{S}}. \quad (3)$$

$\mu_{\text{SnS}_2}$  can be taken from bulk  $\text{SnS}_2$ , or  $G_{\text{SnS}_2}^{\text{bulk}}$  can be used for  $\mu_{\text{SnS}_2}$ . Therefore, using Eq. (3) to eliminate  $\mu_{\text{Sn}}$  in Eq. (1), we obtain the following:

$$\begin{aligned} \gamma_{\text{multilayer ribbon}} &= \frac{1}{2A} [G_{\text{ribbon}}^i - N_{\text{Sn}}(G_{\text{SnS}_2}^{\text{bulk}} - 2\mu_{\text{S}}) - N_{\text{S}}\mu_{\text{S}}] \\ &= \frac{1}{2A} [G_{\text{ribbon}}^i - N_{\text{Sn}}G_{\text{SnS}_2}^{\text{bulk}} - \mu_{\text{S}}(N_{\text{S}} - 2N_{\text{Sn}})]. \end{aligned} \quad (4)$$

From Eq. (4), we can see that the surface formation energy is dependent on  $\mu_{\text{S}}$ . A similar equation can be found for the monolayer ribbon formation energy. At equilibrium, the value of  $\mu_{\text{S}}$  becomes constrained, as discussed in other work [60]. The maximum value of the Sn chemical potential corresponds to bulk Sn:

$$\mu_{\text{Sn}}[\text{max}] = G_{\text{Sn}}^{\text{bulk}}(T, p). \quad (5)$$

Since  $\mu_{\text{S}}$  and  $\mu_{\text{Sn}}$  are constrained by Eq. (3), we can find the minimum possible value of  $\mu_{\text{S}}$  by

$$\mu_{\text{S}}[\text{min}] = \frac{1}{2} [G_{\text{SnS}_2}^{\text{bulk}} - \mu_{\text{Sn}}[\text{max}]]. \quad (6)$$

If the S chemical potential drops below this value, bulk Sn would form since the chemical potential of Sn would be greater than bulk Sn. We used  $\text{S}_2$  as a reference species for the maximum value of the S chemical potential, since gas-phase sulfur is often used for  $\text{SnS}_2$  synthesis [15,59]. The maximum value of  $\mu_{\text{S}}$  was taken to be  $\frac{1}{2}G_{\text{S}_2}$ :

$$\mu_{\text{S}}[\text{max}] = \frac{1}{2}G_{\text{S}_2}. \quad (7)$$

Above this value the S atoms would form  $\text{S}_2$  gas instead of staying on the  $\text{SnS}_2$  edges. We introduce  $\Delta\mu_{\text{S}} = \mu_{\text{S}} - \frac{1}{2}G_{\text{S}_2}$ , which gives us the range of chemical potentials for S:

$$\frac{1}{2} [G_{\text{SnS}_2}^{\text{bulk}} - G_{\text{Sn}}^{\text{bulk}} - G_{\text{S}_2}] < \Delta\mu_{\text{S}} < 0. \quad (8)$$

We thus have a way to determine  $\mu_{\text{S}}$  (or  $\Delta\mu_{\text{S}}$ ) in order to calculate surface formation energies, using, for example, Eq. (4). Entropic and enthalpic energy contributions of gas-phase S are much greater than these contributions from the solid phase, for  $S_{\text{gas}} \gg S_{\text{solid}}$  and  $(PV)_{\text{gas}} \gg (PV)_{\text{solid}}$ . For example, Reuter and Scheffler [60] performed an ab initio thermodynamics study of  $\text{RuO}_2$  up to 1000 K, similar to what we have done in the present work, and found vibrational contributions of the slab to the surface free energy to be less than  $10 \text{ meV}/\text{\AA}^2$ . Alfonso [59] reached a similar conclusion for  $\text{FeS}_2$ , also for simulations up to 1000 K. Other work [61–63] has also shown that solid-phase contributions to free energy changes are typically small so can be ignored. Thus, ignoring entropy and enthalpy for the solid phase allows us to

use DFT-calculated energies in Eq. (8) for the solids, similar to what has been done in previous work [64–67]. We take the energy of  $S_2$  from our DFT calculations. The range of the chemical potential of S thus becomes:

$$-1.31 \text{ eV} \leq \Delta\mu_S \leq 0 \text{ eV}. \quad (9)$$

Reuter and Scheffler [60] indicated that using such an approach gives the range of chemical potentials at 0 K, and that at higher temperatures the chemical potential of gas-phase species may increase on the order of 0.3 to 0.6 eV. We present the surface formation energy results beyond 0 eV in order to account for these elevated temperatures, similar to Reuter and Scheffler [60]. In summary, the surface formation energy of different edge terminations can be found by

$$\gamma_{\text{multilayer ribbons}}^i = \frac{1}{2A} \left[ E_{\text{multilayer ribbons}}^i - N_{\text{Sn}} E_{\text{SnS}_2}^{\text{bulk}} \right. \\ \left. - (N_S - 2N_{\text{Sn}}) \left( \Delta\mu_S + \frac{1}{2} E_{S_2} \right) \right] \quad (10)$$

and

$$\gamma_{\text{multilayer ribbons}}^i = \frac{1}{2L} \left[ E_{\text{monolayer ribbon}}^i - N_{\text{Sn}} E_{\text{SnS}_2}^{\text{bulk}} \right. \\ \left. - (N_S - 2N_{\text{Sn}}) \left( \Delta\mu_S + \frac{1}{2} E_{S_2} \right) \right]. \quad (11)$$

In order to relate the simulation work to real experimental conditions, we correlated the S chemical potentials to sulfur gas at finite temperature and pressure. According to previous studies [68,69], sulfur gas molecules exist as  $S_2$  to  $S_8$ , or a mixture of several species at different temperatures and pressures. At high temperatures and low pressures (which are often used during synthesis), smaller S molecules dominate, especially  $S_2$  [68,70]. We therefore used  $S_2$  as a reference molecule. The chemical potentials at different temperatures were calculated using this equation [60]:

$$\mu_S(T, p) = \mu_S(T, p^\circ) + \frac{1}{2} kT \ln \left( \frac{p}{p^\circ} \right), \quad (12)$$

where  $k$  is the Boltzmann constant and  $\mu_S(T, p^\circ)$  is the chemical potential per atom of  $S_2$  gas at a reference pressure  $p^\circ$ . The chemical potential at the reference pressure can be determined by

$$\mu_S(T, p^\circ) = \frac{1}{2} \mu_{S_2}(0 \text{ K}, p^\circ) + \frac{1}{2} \Delta G(\Delta T, p^\circ, S_2). \quad (13)$$

Taking  $\mu_S(0 \text{ K}) = \frac{1}{2} E_{S_2}$ , we obtain the following:

$$\mu_S(T, p^\circ) = \frac{1}{2} E_{S_2} + \frac{1}{2} [H(T, p^\circ, S_2) - H(0 \text{ K}, p^\circ, S_2)] \\ - \frac{1}{2} T [S(T, p^\circ, S_2) - S(0 \text{ K}, p^\circ, S_2)], \quad (14)$$

where  $\Delta G(\Delta T, p^\circ, S_2)$  is Gibbs free energy of  $S_2$  gas at pressure  $p^\circ$ . We used the JANAF thermochemical data [71] for entropy and enthalpy values used in Eq. (14). Such entropy and enthalpy values include vibrational, rotational, and translational energy contributions. These data were at 0.1 MPa and used as the reference pressure  $p^\circ$ . Equation (14) and the

experimental thermochemical data allow us to relate the S chemical potential to real temperatures and pressures.

### III. RESULTS AND DISCUSSION

#### A. Bulk and monolayer $\text{SnS}_2$ (no edges)

We first describe our results for bulk and monolayer  $\text{SnS}_2$  (no edges). The cells are shown in Fig. 1. We calculated the bulk lattice parameters as  $a = 3.69 \text{ \AA}$ ,  $c = 5.94 \text{ \AA}$ , which agrees well with previous experimental ( $a = 3.65 \text{ \AA}$ ,  $c = 5.90 \text{ \AA}$ ) [26] and simulation ( $a = 3.66 \text{ \AA}$ ,  $c = 5.81 \text{ \AA}$ ) [72] results. Our calculated band gap energy of bulk  $\text{SnS}_2$  is 2.34 eV and is indirect. Figure S4 [51] shows our calculated band structures for bulk and monolayer  $\text{SnS}_2$ . The conduction band minimum (CBM) is located at the L point and the valence band maximum (VBM) is located between the  $M$  and  $\Gamma$  points [33] (see Fig. S4 [51]). According to our calculations, the band gap energy of monolayer  $\text{SnS}_2$  is 2.44 eV. This band gap energy is 0.1 eV larger than that of bulk  $\text{SnS}_2$  [33,38], and monolayer  $\text{SnS}_2$  is an indirect semiconductor where the CBM is located at the M point and VBM is located between the  $\Gamma$  and M points. Both monolayer and bulk  $\text{SnS}_2$  have indirect band gaps according to previous studies [17,33]. This is in contrast to  $\text{MoS}_2$  which has an indirect band gap in the bulk, but a direct band gap when it becomes a monolayer [17,27]. These results match with previous studies, which report similar band structures [36] and indirect band gaps for  $\text{SnS}_2$ .

Our calculated projected DOS of bulk and monolayer  $\text{SnS}_2$  are shown in Fig. S5 [51]. Similar to previous DFT studies [26,33], we found that the valence and conduction bands are composed of hybridized orbitals for  $\text{SnS}_2$ . The conduction bands of both bulk and monolayer are composed of Sn s and S p orbitals, while the valence bands of both bulk and monolayer  $\text{SnS}_2$  are both dominated by S p and Sn d orbitals. Our results agree with previous literature on what is known about  $\text{SnS}_2$ , and also show that both bulk and monolayer  $\text{SnS}_2$  have similar properties.

#### B. Edge Structures of $\text{SnS}_2$

##### 1. Possible S arrangements on the edges

We now turn our attention to  $\text{Sn}_2$  having layers terminated with edges. There are various possible arrangements of  $\text{SnS}_2$  edges with regards to S positions. We describe our efforts to model different surface terminations here. The multilayer and monolayer ribbons we used are shown in Fig. 2, respectively, with the  $(10\bar{1}0)$  facets exposed. At 0% S coverage, only Sn atoms are exposed to the surface. Depending on the S coverage, the edges may have undercoordinated Sn atoms. Each Sn atom in the bulk has a coordination number of 6, while at 0% S coverage, the Sn atoms at the edges have three dangling bonds. At 100% S coverage, each Sn bonds to three surface S atoms, to have a full coordination number of 6.

There are six possible sites for S atoms at the  $(10\bar{1}0)$  edges, as Fig. 3(a) shows. Sites 1 and 2 correspond to positions occurring in bulk  $\text{SnS}_2$ , and are named in-registry site 1 (IR1) and in-registry site 2 (IR2). If we cut bulk  $\text{SnS}_2$  and do not allow relaxation, the S atoms would be in IR1 and IR2 sites. Site 3 bridges two Sn atoms, and is named a bridge site (B). Site 4 is directly on top of a Sn atom, and is named the top

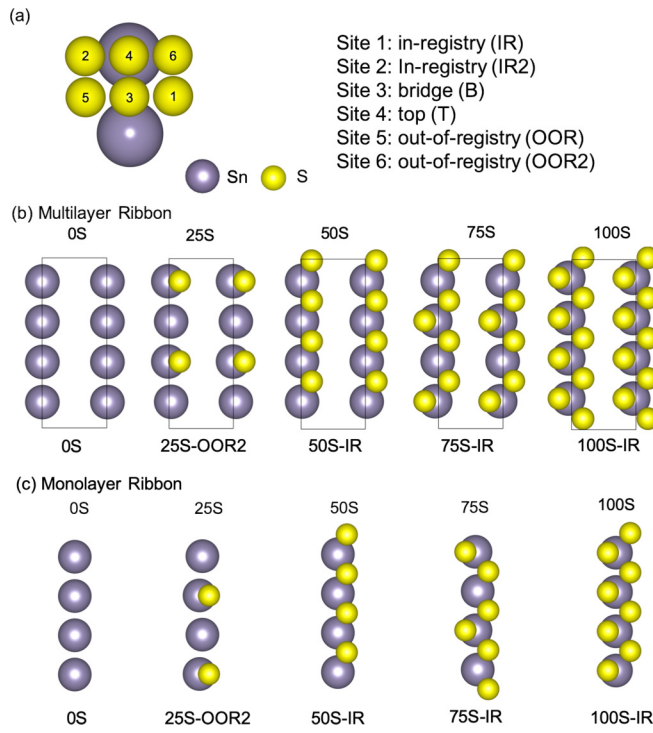


FIG. 3. (a) Different possible S positions on the surface terminations. Top views of the most stable configurations at different S coverage for (b) multilayer edges and (c) monolayer edges are given. Indicated are the final converged configurations of the S atoms.

site (T). Sites 5 and 6 are the sites that are at the opposite positions of IR1 and IR2, and are named out-of-registry site 1 (OOR1) and out-of-registry site 2 (OOR2). We have four Sn atoms at each edge in the supercell, and eight S atoms would be equivalent to full (100S) coverage. In other words, for our chosen simulation cell eight S atoms at an edge corresponds to 100% S coverage, while six S atoms corresponds to 75% S coverage, etc. We modeled a range of S coverage and also several possible initial configurations of the S atoms at the edges, which are summarized in Table I. We modeled edges with 0%, 25%, 75%, and 100% S coverage for both multilayer and monolayer  $\text{SnS}_2$  ribbons, as shown in Figs 3(b) and 3(c). A ribbon with 50% S coverage is a fully stoichiometric ribbon ( $\text{SnS}_2$ ). We modeled two different sites when the S coverage at an edge was more than 50%. For example, 75% S covered edges could have both IR and OOR sites occupied at the same time. In this case, if there are more IR-S atoms than OOR-S atoms, this would be called a 75S-IR edge. If there are more OOR-S than IR-S atoms this would be called a 75S-OOR edge.

We modeled several initial configurations for the edges, and then allowed the ribbons to relax. Table I indicates all of the configurations before and after relaxation. We modeled six different initial configurations for 25S, six for 50S, three for 75S, and two for 100S. We also indicate the final configurations. On some surfaces the S atoms rearranged to form different structures than the initial configurations. For example, the 50S-IR2 configuration converged to the 50S-OOR2 configuration after geometry optimization. Some initial configurations did not converge after more than several thousand

TABLE I. Adsorption energies and optimized surface configurations for multilayer and monolayer  $\text{SnS}_2$  ribbons up to 100% S coverage. Initial and final (after geometry optimization) configurations are indicated. Adsorption energies were calculated using Eq. (15). Provided are the adsorption energies per S atom, and the total adsorption energy per edge (adsorption energy per S atom multiplied by total number of S atoms). The nomenclature for edge configurations are given in Fig. 3(a). Certain edge configurations did not converge after several thousand geometry optimization steps, and are indicated by dashes.

Initial configuration	Multilayer edges			Monolayer edges		
	Final configuration	Adsorption energy (eV/atom)	Total adsorption energy (eV)	Final configuration	Adsorption energy (eV/atom)	Total adsorption energy (eV)
100S-IR	100S-IR	0.23	1.84	100S-IR	0.31	2.48
100S-OOR	—			—		
75S-IR	75S-IR	-0.10	-0.6	75S-IR	-0.02	-0.12
75S-IR2	75S-IR2	0.24	1.44	—		
75S-OOR	—			—		
50S-IR	50S-IR	-0.72	-2.88	50S-IR	-0.64	-2.56
50S-IR2	50S-OOR2	0.06	0.24	50S-OOR2	0.13	0.52
50S-OOR	—			—		
50S-OOR2	50S-OOR2	0.06	0.24	50S-OOR2	0.13	0.52
50S-B	50S-IR	-0.72	-2.88	50S-IR	-0.64	-2.56
50S-T	50S-OOR2	0.06	0.24	50S-OOR2	0.13	0.52
25S-IR	25S-IR	0.28	0.56	25S-IR	0.38	0.76
25S-IR2	25S-OOR2	-0.32	-0.64	25S-OOR2	-0.23	-0.46
25S-OOR	25S-OOR	0.79	1.58	25S-IR	0.38	0.76
25S-OOR2	25S-OOR2	-0.32	-0.64	25S-OOR2	-0.23	-0.46
25S-B	25S-IR	0.29	0.58	25S-IR	0.38	0.76
25S-T	25S-OOR2	-0.32	-0.64	25S-OOR2	-0.23	-0.46
0S	0S	0	0	0S	0	0

geometry steps, indicating those configurations are not likely stable.

To determine the sulfur adsorption energy for each S coverage, we calculated the S adsorption energies at 0 K using the reaction:  $0S + \frac{x}{2}S_2 \rightarrow yS$ , where 0S is the multilayer or monolayer ribbon at 0% S coverage (no S on the edge). yS is the multilayer or monolayer ribbon at y% (y = 25, 50, 75, and 100) S coverage. x is the number of S atoms added to the edge of the yS ribbon.  $S_2$  was chosen as a reference S molecule in the vapor phase for consistency. Accordingly, the adsorption energies of S were calculated by the following equation:

$$E(\text{adsorption})_{(yS)} = \frac{E_{yS} - E_{0S} - \frac{x}{2}E_{S_2}}{x}. \quad (15)$$

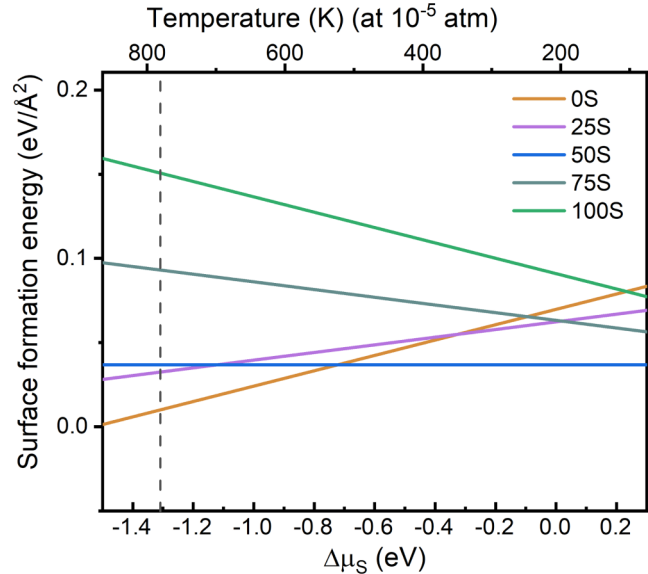
$E_{yS}$  is the total energy of the ribbons at y% S coverage. x is the number of sulfur atoms adsorbed at the edges.  $E_{S_2}$  is the total energy of a  $S_2$  molecule. The adsorption energies were normalized by the number of S atoms added to the surfaces, so that the adsorption energy will be in eV/atom. Table I provides adsorption energies for S, as well as the number of S atoms on the edges for each S coverage.

The results show that the most stable configurations at each different S coverage are 25S-OOR2, 50S-IR, 75S-IR, and 100S-IR, which are shown in Fig. 3. Thus we found that the most stable orientation of S atoms at 25% S coverage had the S atoms out of registry compared to bulk positions. This orientation could be termed a reconstruction due to the shifting of the S atoms away from bulk positions. Similar shifting of S atoms at edges has been observed in  $\text{MoS}_2$  [30,73]. On the other hand, for higher coverages (50S and above) the most stable S configuration occurred with the S atoms in-registry (bulk S atom orientation). We found no evidence in the literature for reconstructions being observed for  $\text{SnS}_2$  edges. Since the 50S coverage was the most stable coverage and had no reconstructions, our results are consistent with what is known in the literature. Furthermore, the 50S-IR edges are the most stable for both multilayer and monolayer at 0 K, since they have lowest total adsorption energies as Table I shows. This is the stoichiometric edge, so from a chemistry viewpoint should be very stable. The high coverage surfaces were not stable or only weakly stable. For several of the high coverage surfaces (i.e., 100S) during the geometry optimization,  $S_2$  molecules would occasionally leave the surface, dissociating from the  $\text{SnS}_2$  surface. This reinforces the notion that high coverage of S is unstable on the  $\text{SnS}_2$  edges. These results show that, in general, S atoms are more likely to occupy the in-registry sites of the edges, with the exception of OOR2 sites being more favorable over the 25S edges. IR-S atoms have the same positions as S atoms in bulk  $\text{SnS}_2$ , which explains why they are so stable when adsorbed on the edges. In addition, the fact that the stable edge configurations of multilayer and monolayer ribbons are the same suggests that the van der Waals force between  $\text{SnS}_2$  layers do not significantly affect the edge configurations.

## 2. Thermodynamic considerations of edge structures

So far, we determined the most stable arrangement of S atoms at the edges for various S coverages at 0 K. Next, we aim to determine the relative stability of different surfaces

## (a) multilayer ribbon



## (b) monolayer ribbon

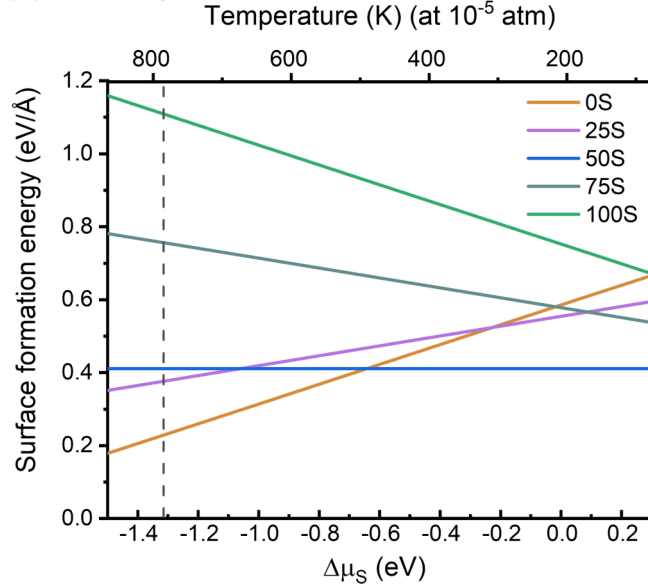


FIG. 4. Surface free energies of multilayer (a) and monolayer (b)  $\text{SnS}_2$  ribbons at different S chemical potentials. The corresponding temperatures (top x axis) are determined by the chemical potential of  $S_2$  gas at  $10^{-5}$  atm. The dashed vertical line represents the minimum value of  $\Delta\mu_S$  when using  $S_2$  as a reference.

as a function of S chemical potential, which can be related to actual temperature and pressure. We calculated the surface free energy as function of S chemical potential for multilayer and monolayer  $\text{SnS}_2$  ribbons using Eq. (4). These results are given in Fig. 4.

The slope of each surface grand potential line is determined by  $\frac{N_S - 2N_{\text{Sn}}}{2A}$ , as rearranging Eq. (10) shows

$$\gamma^i = \frac{1}{2A} [E_{\text{ribbon}}^i - N_{\text{Sn}} E_{\text{SnS}_2}^{\text{bulk}}] + \frac{(N_S - 2N_{\text{Sn}})}{2A} \frac{1}{2} E_{S_2} - \frac{(N_S - 2N_{\text{Sn}})}{2A} \Delta\mu_S. \quad (16)$$

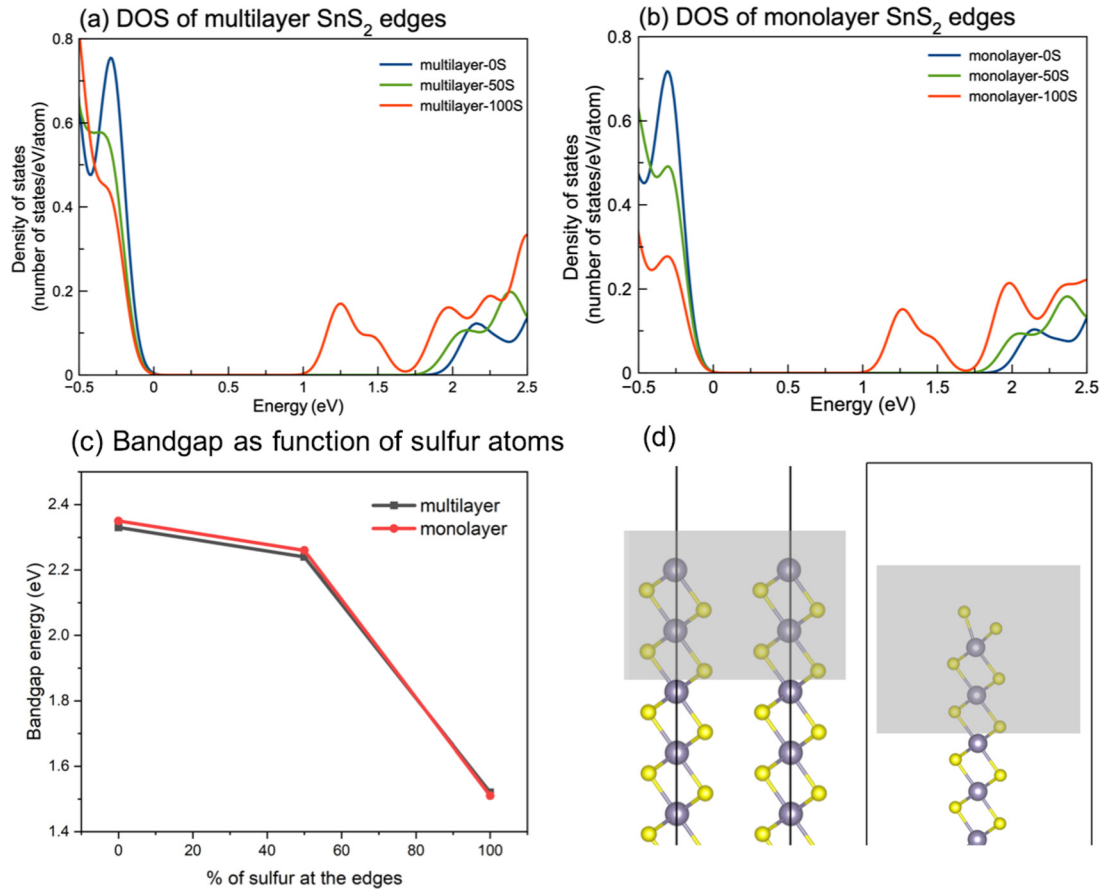


FIG. 5. Density of states of (a) multilayer and (b) monolayer SnS<sub>2</sub> ribbons as calculated using the HSE06 functional. The valence band edge is set at 0 eV. (c) The band gap energy as a function of sulfur coverage. For reference, the calculated band gap energies of bulk SnS<sub>2</sub> and monolayer SnS<sub>2</sub> (no edges) are 2.34 and 2.44 eV. (d) Side view of multilayer and monolayer slabs. Grey lines indicate the cell edges. The shaded atoms were used to calculate the DOS representing edge atoms.

A similar rearrangement can be found using Eq. (11) for monolayer ribbons. Because of this slope, the surfaces with more sulfur atoms (N<sub>S</sub>) have more negative slopes and become more favorable with increasing sulfur chemical potential. The lines with negative slope correspond to the edges with excess S atoms (75S and 100S), while those with positive slope correspond to the edges with deficient S atoms (0S and 25S). A slope of 0 corresponds to the stoichiometric edge (50S). Therefore 75S and 100S edges are more stable in the sulfur rich region, and 0S and 25S edges are more favorable in the sulfur poor region.

The edge coverage with the lowest surface free energy is the most stable at a given S chemical potential. Hence, from Fig. 4, we can conclude that multilayer and monolayer SnS<sub>2</sub> edges will adopt a 0S coverage at low  $\mu_S$  and 50S coverage for higher  $\mu_S$  values. 75S and 100S coverage are not stable at any of the chemical potential ranges. Interestingly, the 25S is also not stable, so that the coverage jumps from 0 to 50S abruptly. The most stable arrangement of S atoms for the 25S surface has S atoms in the OOR2 arrangement, unlike any other surface, which could explain why 25S coverage would not be observed for these ribbons. We point out that the most stable edge terminations are nearly the same for the monolayer and multilayer ribbons, which indicates that interactions between layers do not affect edge stability.

We also wanted to understand these results in the context of sulfur at different temperatures and pressures. We chose molecular sulfur (S<sub>2</sub>) at 10<sup>-5</sup> atm as our reference state. In our previous experiments [15] the SnS<sub>2</sub> nanoflakes were synthesized at 723 K and 10<sup>-5</sup> atm which corresponds to  $\Delta\mu_S$  of -1.2 eV. The corresponding temperatures of S<sub>2</sub> molecules at 10<sup>-5</sup> are given in the upper x axis of Fig. 4. Table S2 [51] provides  $\mu_S$  values for a range of pressures and temperatures that may correspond to a variety of other environmental or synthesis conditions. This allows connection of our calculated surface grand potential to experiment. According to Fig. 4 the most stable nanoflakes that we synthesized in our previous work [15] would have 0% S covered edges, at least during synthesis. If the flakes could be synthesized at lower temperatures, then 50S edges may form, but at lower temperatures diffusion limitations may limit nanoflake synthesis.

We also considered the possibility of other sulfur molecules. Table S3 [51] shows chemical potentials for S<sub>8</sub>, rather than S<sub>2</sub>. In reality sulfur gas will be a mixture of different molecules [68], and depending on temperature/pressure, different sulfur molecules will dominate the gas phase. Table S3 [51] gives chemical potentials for S<sub>8</sub> molecules. Unlike S<sub>2</sub>, the chemical potentials span a very narrow range, and in the presence of S<sub>8</sub> the SnS<sub>2</sub> surface would

adopt a 50S termination, except for very high temperatures.

### C. Electronic properties of the edges

The electronic properties of  $\text{SnS}_2$  edges are important for many applications. Here we present the calculated DOS and band structures of the most stable multilayer and monolayer  $\text{SnS}_2$  edges (as determined in Sec. III B). Figure 5 shows the density of states of multilayer and monolayer  $\text{SnS}_2$  edges. The atoms in the top seventh to eight atomic layers were taken as edge atoms, and used to obtain the DOS and band structure of the edges [see Fig. 5(d)]. Figure 5 shows that the band gap energies of the edges are smaller than the band gap energies of bulk  $\text{SnS}_2$  (2.34 eV), and that the band gap energy decrease with increasing S coverage. The band gap energies of both multilayer and monolayer 0S and 50S edges are slightly smaller than those of the bulk and monolayer  $\text{SnS}_2$  without edges, while the band gap energies of 100S edges are around 0.7 eV smaller than that of the bulk and monolayer  $\text{SnS}_2$  without edges. These results show that by controlling the S coverage of the edges of  $\text{SnS}_2$  flakes, the band gap energy of the edges can be controlled, which may modulate photoabsorption behavior. According to the DOS plots, the edges of  $\text{SnS}_2$  are still semiconducting, no matter the S coverage. This is in contrast to the metallic edges of typical 2D sulfides, such as 2H-MoS<sub>2</sub> [28,29]. The semiconducting edges of  $\text{SnS}_2$  could avoid the short circuit issue that MoS<sub>2</sub> might have in FETs. Furthermore, the charge recombination rate at the semiconducting edges could be smaller than at metallic edges, indicating  $\text{SnS}_2$  could be a promising photovoltaic or photocatalytic material.

Direct band gap semiconductors have better photoluminescence [27] and may be more suitable in photovoltaic applications due to higher photoabsorption [31,74]. We found that multilayer and monolayer-50S edges are unlike the basal planes, in that they both edges have direct band gaps (Fig. 6), while multilayer and monolayer 0S and 100S edges have indirect band gaps, similar to bulk  $\text{SnS}_2$ . This is important, because it indicates that photoabsorption should be enhanced at the 50 S edges compared to bulk  $\text{SnS}_2$  or at the basal planes. However, 50 S edges may also enable more facile charge recombination, which could be detrimental. These results indicate that the band electronic properties can be modulated by controlling the edge configurations.

### D. Reactivity of edges

The edges of  $\text{SnS}_2$  may be especially reactive sites for photocatalysis or electrocatalysis, especially when compared to the basal planes. We accordingly simulated hydrogen and oxygen dissociative adsorption on the 0S and 50S edges (the two-most stable edges) as well at basal planes in order to probe their potential reactivity. Certainly these results are not complete in defining the catalytic or reactive nature of these edges, but could provide important insight on edge reactivity. We modeled H or O atom adsorption at various locations on the edges, either interacting with Sn or S atoms. For instance, we modeled several configurations with a single H atom on top of S, an H atom in between two Sn atoms, or an H

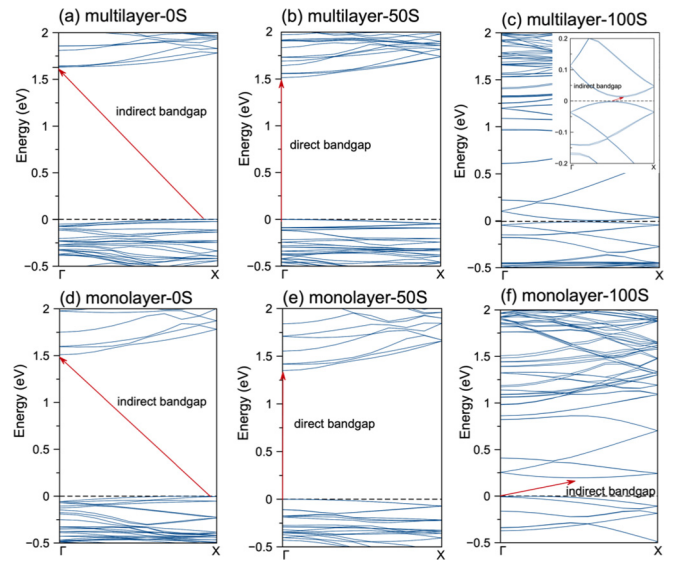


FIG. 6. Calculated band structures of multilayer and monolayer ribbons. The valence band maximum are set at 0 eV. The inset of (c) shows a zoomed in region of the band gap. Results are from using the PBE functional, which is why band gap energies are underestimated. As discussed in the Methodology, PBE and HSE06 give qualitative agreement for band structures (see Fig. S1 [51]), even if PBE underestimates band gap energies.

atom in between two S atoms. Figures 7 and 8 show the final configurations for H and O adsorption. Reaction energies were calculated by

$$E_{\text{ad}} = E_{\text{H+ribbon}} - E_{\text{ribbon}} - \frac{1}{2}E_{\text{H}_2} \quad (17)$$

or

$$E_{\text{ad}} = E_{\text{O+ribbon}} - E_{\text{ribbon}} - \frac{1}{2}E_{\text{O}_2}. \quad (18)$$

The dissociative adsorption energies for H<sub>2</sub> were all endothermic, although the values were just barely endothermic over the 50S edges. We could thus consider the H dissociation

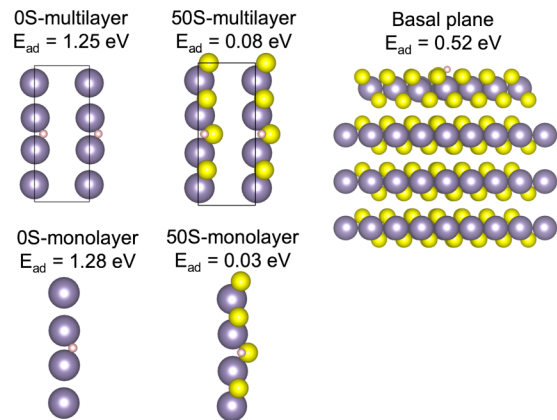


FIG. 7. Hydrogen dissociative adsorption results on the 0S edges and 50S edges. Shown are the most stable configurations for adsorbed H atoms along with adsorption energies. For comparison, dissociative adsorption results of H are given for the basal plane.

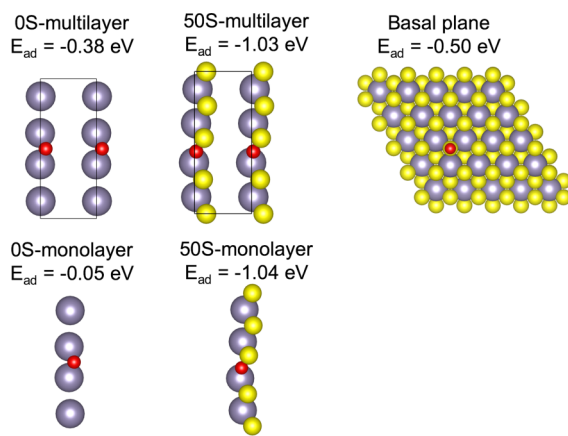


FIG. 8. Oxygen dissociative adsorption results on the 0S edges and 50S edges. Shown are the most stable configurations for adsorbed O atoms along with adsorption energies. For comparison, dissociative adsorption results of O are given for the basal plane.

process to be thermodynamically neutral over the 50s edges, especially when considering any errors that may be in the calculated dissociation energies due to DFT approximations. The 50s surface provides under-coordinated S atoms for the hydrogen to dissociate at. Dissociative adsorption is weakest on the 0S edge, even more so than the basal planes. This may seem surprising, but adsorption over the 0S surface involves Sn-H bonds, while over the basal planes involves S-H bonds. S-H bonds are stronger than Sn-H bonds, which explains these adsorption energies. Chia *et al.* [44] modeled H<sub>2</sub> dissociative adsorption over SnS<sub>2</sub> edges to obtain an adsorption energy of  $\sim 0.4$  eV. This differs from our value of 0.08 eV, but we both still obtained endothermic dissociation energies. Such differences could be attributable to the choice of exchange-correlation functional or other simulation parameters. It is also unclear what edge structures they modeled. For comparison, hydrogen dissociative adsorption over MoS<sub>2</sub> was calculated to be exothermic [75,76], which indicates that edges may have different properties for dichalcogenides.

We also modeled O<sub>2</sub> dissociation, and this process was always exothermic over SnS<sub>2</sub> as Figure 8 shows, in contrast

to H dissociation. O<sub>2</sub> dissociation is about two times more exothermic over the 50s edges compared to the basal planes, indicating that edges are more reactive than basal planes, similar to what was observed for H dissociation. Also similar to H<sub>2</sub> dissociation, 0S edges are less reactive than 50s edges. Our results indicate that synthesis of SnS<sub>2</sub>, especially under certain synthesis conditions, may form reactive flakes with edges that may be more reactive than basal planes. Such edges which may be key reaction sites. This may partially explain the experimental observations that edge-oriented SnS<sub>2</sub> nanoflakes have better photo-electro-chemical performance than single crystal SnS<sub>2</sub> [15,32].

#### IV. CONCLUSIONS

We modeled edges of SnS<sub>2</sub> using DFT to find their stable configurations at different S coverage. We modeled both monolayer and multilayer ribbons (with edges), as well as bulk and monolayer Sn<sub>2</sub> (no edges). We also included thermodynamic analysis to determine edge stability at different pressures and temperatures. Our results show that 0S and 50S edges are most stable, and that higher S coverage are unstable. According to our thermodynamic calculations, the as-synthesized SnS<sub>2</sub> can have different edge terminations under different experimental condition, which means one can control terminations of SnS<sub>2</sub> edges by controlling experimental conditions. In contrast to the metallic edges of 2H-MoS<sub>2</sub>, SnS<sub>2</sub> has semiconducting edges, indicating promising properties for photovoltaic and photocatalytic applications. This paper provides fundamental knowledge of multilayer and monolayer SnS<sub>2</sub> edges including their atomic configurations and electronic structures, which is important for research and applications involving SnS<sub>2</sub>.

#### ACKNOWLEDGMENTS

The authors acknowledge support from Worcester Polytechnic Institute, the Materials Science and Engineering Graduate Program of the Mechanical Engineering Department at Worcester Polytechnic Institute. This work was supported by the National Science Foundation under grant No. 1704975.

---

[1] C. Lee, X. Wei, J. W. Kysar, and J. Hone, Measurement of the elastic properties and intrinsic strength of monolayer graphene, *Science* **321**, 385 (2008).

[2] F. Schedin, A. Geim, S. Morozov, E. Hill, P. Blake, M. Katsnelson, and K. Novoselov, Detection of individual gas molecules adsorbed on graphene, *Nat. Mater.* **6**, 652 (2007).

[3] R. R. Nair, P. Blake, A. N. Grigorenko, K. S. Novoselov, T. J. Booth, T. Stauber, N. M. Peres, and A. K. Geim, Fine structure constant defines visual transparency of graphene, *Science* **320**, 1308 (2008).

[4] K. S. Novoselov, A. K. Geim, S. V. Morozov, D. Jiang, Y. Zhang, S. V. Dubonos, I. V. Grigorieva, and A. A. Firsov, Electric field effect in atomically thin carbon films, *Science* **306**, 666 (2004).

[5] R. Prins, V. De Beer, and G. Somorjai, Structure and function of the catalyst and the promoter in Co-Mo hydrodesulfurization catalysts, *Catalysis Rev.* **31**, 1 (1989).

[6] M. Salmeron, G. Somorjai, A. Wold, R. Chianelli, and K. Liang, The adsorption and binding of thiophene, butene and H<sub>2</sub>S on the basal plane of MoS<sub>2</sub> single crystals, *Chem. Phys. Lett.* **90**, 105 (1982).

[7] T. F. Jaramillo, K. P. Jørgensen, J. Bonde, J. H. Nielsen, S. Horch, and I. Chorkendorff, Identification of active edge sites for electrochemical H<sub>2</sub> evolution from MoS<sub>2</sub> nanocatalysts, *Science* **317**, 100 (2007).

[8] S. M. Ahmed and H. Gerischer, Influence of crystal surface orientation on redox reactions at semiconducting MoS<sub>2</sub>, *Electrochim. Acta* **24**, 705 (1979).

[9] H. Fang, S. Chuang, T. C. Chang, K. Takei, T. Takahashi, and A. Javey, High-performance single layered WSe<sub>2</sub> *p*-FETs with chemically doped contacts, *Nano Lett.* **12**, 3788 (2012).

[10] W. Zhao, Z. Ghorannevis, L. Chu, M. Toh, C. Kloc, P.-H. Tan, and G. Eda, Evolution of electronic structure in atomically thin sheets of WS<sub>2</sub> and WSe<sub>2</sub>, *ACS Nano* **7**, 791 (2012).

[11] K.-K. Liu, W. Zhang, Y.-H. Lee, Y.-C. Lin, M.-T. Chang, C.-Y. Su, C.-S. Chang, H. Li, Y. Shi, H. Zhang, *et al.*, Growth of large-area and highly crystalline MoS<sub>2</sub> thin layers on insulating substrates, *Nano Lett.* **12**, 1538 (2012).

[12] G. Frey, R. Tenne, M. Matthews, M. Dresselhaus, and G. Dresselhaus, Optical properties of MS<sub>2</sub> (M = Mo, W) inorganic fullerenelike and nanotube material optical absorption and resonance raman measurements, *J. Mater. Res.* **13**, 2412 (1998).

[13] A. Beal, H. Hughes, and W. Liang, The reflectivity spectra of some group va transition metal dichalcogenides, *J. Phys. C* **8**, 4236 (1975).

[14] J. Yu, C.-Y. Xu, F.-X. Ma, S.-P. Hu, Y.-W. Zhang, and L. Zhen, Monodisperse SnS<sub>2</sub> nanosheets for high-performance photocatalytic hydrogen generation, *ACS Appl. Mater. Interfaces* **6**, 22370 (2014).

[15] B. Giri, M. Masroor, T. Yan, K. Kushnir, A. D. Carl, C. Doiron, H. Zhang, Y. Zhao, A. McClelland, G. A. Tompsett, *et al.*, Balancing light absorption and charge transport in vertical SnS<sub>2</sub> nanoflake photoanodes with stepped layers and large intrinsic mobility, *Adv. Energy Mater.* **9**, 1901236 (2019).

[16] G. Liu, Y. Qiu, Z. Wang, J. Zhang, X. Chen, M. Dai, D. Jia, Y. Zhou, Z. Li, and P. Hu, Efficiently synergistic hydrogen evolution realized by trace amount of Pt-decorated defect-rich SnS<sub>2</sub> nanosheets, *ACS Appl. Mater. Interfaces* **9**, 37750 (2017).

[17] Y. Huang, E. Sutter, J. T. Sadowski, M. Cotlet, O. L. Monti, D. A. Racke, M. R. Neupane, D. Wickramaratne, R. K. Lake, B. A. Parkinson, *et al.*, Tin disulfide- an emerging layered metal dichalcogenide semiconductor: materials properties and device characteristics, *ACS Nano* **8**, 10743 (2014).

[18] L. Gao, C. Chen, K. Zeng, C. Ge, D. Yang, H. Song, and J. Tang, Broadband, sensitive and spectrally distinctive SnS<sub>2</sub> nanosheet/PbS colloidal quantum dot hybrid photodetector, *Light: Science Applications* **5**, e16126 (2016).

[19] W. Chu, X. Li, S. Li, J. Hou, Q. Jiang, and J. Yang, High-performance flexible perovskite solar cells with a metal sulfide electron transport layer of SnS<sub>2</sub> by room-temperature vacuum deposition, *ACS Applied Energy Mater.* **2**, 382 (2018).

[20] M. Liu, J. Yang, Q. Qu, P. Zhu, and W. Li, High-quality SnO<sub>2</sub>@SnS<sub>2</sub> core-shell heterojunctions: Designed construction, mechanism and photovoltaic applications, *J. Power Sources* **273**, 848 (2015).

[21] B. Luo, Y. Fang, B. Wang, J. Zhou, H. Song, and L. Zhi, Two dimensional graphene–SnS<sub>2</sub> hybrids with superior rate capability for lithium ion storage, *Energy Environ. Sci.* **5**, 5226 (2012).

[22] J.-w. Seo, J.-t. Jang, S.-w. Park, C. Kim, B. Park, and J. Cheon, Two-dimensional SnS<sub>2</sub> nanoplates with extraordinary high discharge capacity for lithium ion batteries, *Adv. Mater.* **20**, 4269 (2008).

[23] H. Song, S. Li, L. Gao, Y. Xu, K. Ueno, J. Tang, Y. Cheng, and K. Tsukagoshi, High-performance top-gated monolayer SnS<sub>2</sub> field-effect transistors and their integrated logic circuits, *Nanoscale* **5**, 9666 (2013).

[24] J. Z. Ou, W. Ge, B. Carey, T. Daeneke, A. Rotbart, W. Shan, Y. Wang, Z. Fu, A. F. Chrimes, W. Wlodarski, *et al.*, Physisorption-based charge transfer in two-dimensional SnS<sub>2</sub> for selective and reversible NO<sub>2</sub> gas sensing, *ACS Nano* **9**, 10313 (2015).

[25] R. Gupta and F. Yakuphanoglu, Photoconductive schottky diode based on Al/p-Si/SnS<sub>2</sub>/Ag for optical sensor applications, *Solar Energy* **86**, 1539 (2012).

[26] L. A. Burton, T. J. Whittles, D. Hesp, W. M. Linhart, J. M. Skelton, B. Hou, R. F. Webster, G. O'Dowd, C. Reece, D. Cherns, *et al.*, Electronic and optical properties of single crystal SnS<sub>2</sub>: an earth-abundant disulfide photocatalyst, *J. Mater. Chem. A* **4**, 1312 (2016).

[27] A. Splendiani, L. Sun, Y. Zhang, T. Li, J. Kim, C.-Y. Chim, G. Galli, and F. Wang, Emerging photoluminescence in monolayer MoS<sub>2</sub>, *Nano Lett.* **10**, 1271 (2010).

[28] M. V. Bollinger, J. V. Lauritsen, K. W. Jacobsen, J. K. Nørskov, S. Helveg, and F. Besenbacher, One-Dimensional Metallic Edge States in MoS<sub>2</sub>, *Phys. Rev. Lett.* **87**, 196803 (2001).

[29] Y. Li, Z. Zhou, S. Zhang, and Z. Chen, MoS<sub>2</sub> nanoribbons: high stability and unusual electronic and magnetic properties, *J. Am. Chem. Soc.* **130**, 16739 (2008).

[30] J. Lauritsen, M. Bollinger, E. Lægsgaard, K. W. Jacobsen, J. K. Nørskov, B. Clausen, H. Topsøe, and F. Besenbacher, Atomic-scale insight into structure and morphology changes of MoS<sub>2</sub> nanoclusters in hydrotreating catalysts, *J. Catal.* **221**, 510 (2004).

[31] M.-L. Tsai, S.-H. Su, J.-K. Chang, D.-S. Tsai, C.-H. Chen, C.-I. Wu, L.-J. Li, L.-J. Chen, and J.-H. He, Monolayer MoS<sub>2</sub> heterojunction solar cells, *ACS Nano* **8**, 8317 (2014).

[32] G. Liu, Z. Li, T. Hasan, X. Chen, W. Zheng, W. Feng, D. Jia, Y. Zhou, and P. Hu, Vertically aligned two-dimensional SnS<sub>2</sub> nanosheets with a strong photon capturing capability for efficient photoelectrochemical water splitting, *J. Mater. Chem. A* **5**, 1989 (2017).

[33] J. M. Gonzalez and I. I. Oleynik, Layer-dependent properties of SnS<sub>2</sub> and SnSe<sub>2</sub> two-dimensional materials, *Phys. Rev. B* **94**, 125443 (2016).

[34] H. L. Zhuang and R. G. Hennig, Theoretical perspective of photocatalytic properties of single-layer SnS<sub>2</sub>, *Phys. Rev. B* **88**, 115314 (2013).

[35] Y. Seminovski, P. Palacios, and P. Wahnón, Effect of van der Waals interaction on the properties of SnS<sub>2</sub> layered semiconductor, *Thin Solid Films* **535**, 387 (2013).

[36] L. Sun, W. Zhou, Y. Liu, D. Yu, Y. Liang, and P. Wu, Theoretical perspective on the electronic, magnetic and optical properties of Zn-doped monolayer SnS<sub>2</sub>, *Appl. Surf. Sci.* **389**, 484 (2016).

[37] L. Sun, W. Zhou, Y. Liang, L. Liu, and P. Wu, Magnetic properties in Fe-doped SnS<sub>2</sub>: Density functional calculations, *Comput. Mater. Sci.* **117**, 489 (2016).

[38] H. Lu, Y. Guo, and J. Robertson, Band edge states, intrinsic defects, and dopants in monolayer HfS<sub>2</sub> and SnS<sub>2</sub>, *Appl. Phys. Lett.* **112**, 062105 (2018).

[39] B. Sainbileg, Y.-R. Lai, L.-C. Chen, and M. Hayashi, The dual-defective SnS<sub>2</sub> monolayers: promising 2d photocatalysts for overall water splitting, *Phys. Chem. Chem. Phys.* **21**, 26292 (2019).

[40] S. U. Rehman and Z. J. Ding, Enhanced electronic and optical properties of three tmd heterobilayers, *Phys. Chem. Chem. Phys.* **20**, 16604 (2018).

[41] Y. Liu, G. Qiu, D. Kong, B. Hu, Y. Li, J. Su, and C. Xia, Strain effect on SnS<sub>2</sub> nanoribbons: Robust direct bandgap of zigzag-

edge and sensitive indirect semiconductor with armchair-edge states, *Superlattices Microstruct.* **111**, 480 (2017).

[42] L. Li, H. Li, J. Zhou, J. Lu, R. Qin, Z. Gao, and W. N. Mei, Electronic structure and stability of ultranarrow single-layer SnS<sub>2</sub> nanoribbons: A first-principles study, *Journal of Computational and Theoretical Nanoscience* **7**, 2100 (2010).

[43] K. Tu, F. Li, and Z. Chen, Enhanced lithium adsorption/diffusion and improved li capacity on SnS<sub>2</sub> nanoribbons: A computational investigation, *J. Mater. Res.* **31**, 878 (2016).

[44] X. Chia, P. Lazar, Z. Sofer, J. Luxa, and M. Pumera, Layered SnS versus SnS<sub>2</sub>: Valence and structural implications on electrochemistry and clean energy electrocatalysis, *J. Phys. Chem. C* **120**, 24098 (2016).

[45] G. Kresse and J. Hafner, *Ab initio* molecular dynamics for liquid metals, *Phys. Rev. B* **47**, 558 (1993).

[46] G. Kresse and J. Hafner, *Ab initio* molecular-dynamics simulation of the liquid-metal–amorphous-semiconductor transition in germanium, *Phys. Rev. B* **49**, 14251 (1994).

[47] G. Kresse and J. Furthmüller, Efficient iterative schemes for *ab initio* total-energy calculations using a plane-wave basis set, *Phys. Rev. B* **54**, 11169 (1996).

[48] G. Kresse and J. Furthmüller, Efficiency of *ab-initio* total energy calculations for metals and semiconductors using a plane-wave basis set, *Comput. Mater. Sci.* **6**, 15 (1996).

[49] J. P. Perdew, K. Burke, and M. Ernzerhof, Generalized Gradient Approximation Made Simple, *Phys. Rev. Lett.* **77**, 3865 (1996).

[50] J. Heyd, G. E. Scuseria, and M. Ernzerhof, Hybrid functionals based on a screened coulomb potential, *J. Chem. Phys.* **118**, 8207 (2003).

[51] See Supplemental Material at <http://link.aps.org/supplemental/10.1103/PhysRevB.102.155306> for more computational details and results.

[52] Y. Hinuma, G. Pizzi, Y. Kumagai, F. Oba, and I. Tanaka, Band structure diagram paths based on crystallography, *Comput. Mater. Sci.* **128**, 140 (2017).

[53] S. Grimme, J. Antony, S. Ehrlich, and H. Krieg, A consistent and accurate *ab initio* parametrization of density functional dispersion correction (DFT-D) for the 94 elements h-pu, *J. Chem. Phys.* **132**, 154104 (2010).

[54] S. Grimme, S. Ehrlich, and L. Goerigk, Effect of the damping function in dispersion corrected density functional theory, *J. Comput. Chem.* **32**, 1456 (2011).

[55] M. Li, E. Liu, H. Hu, S. Ouyang, H. Xu, and D. Wang, Surfactant-free synthesis of single crystalline SnS<sub>2</sub> and effect of surface atomic structure on the photocatalytic property, *Int. J. Photoenergy* **2014** 394146 (2014).

[56] X.-G. Wang, W. Weiss, S. K. Shaikhutdinov, M. Ritter, M. Petersen, F. Wagner, R. Schlögl, and M. Scheffler, The Hematite ( $\alpha$ -Fe<sub>2</sub>O<sub>3</sub>)(0001) Surface: Evidence for Domains of Distinct Chemistry, *Phys. Rev. Lett.* **81**, 1038 (1998).

[57] X.-G. Wang, A. Chaka, and M. Scheffler, Effect of the environment on  $\alpha$ -Al<sub>2</sub>O<sub>3</sub> (0001) surface structures, *Phys. Rev. Lett.* **84**, 3650 (2000).

[58] F. Bottin, F. Finocchi, and C. Noguera, Stability and electronic structure of the (1 × 1) SrTiO<sub>3</sub> (110) polar surfaces by first-principles calculations, *Phys. Rev. B* **68**, 035418 (2003).

[59] D. R. Alfonso, Computational investigation of fes2 surfaces and prediction of effects of sulfur environment on stabilities, *J. Phys. Chem. C* **114**, 8971 (2010).

[60] K. Reuter and M. Scheffler, Composition, structure, and stability of RuO<sub>2</sub>(110) as a function of oxygen pressure, *Phys. Rev. B* **65**, 035406 (2001).

[61] N. İnoğlu and J. R. Kitchin, Atomistic thermodynamics study of the adsorption and the effects of water-gas shift reactants on cu catalysts under reaction conditions, *J. Catal.* **261**, 188 (2009).

[62] N. Seriani, W. Pompe, and L. C. Ciacchi, Catalytic oxidation activity of Pt<sub>3</sub>O<sub>4</sub> surfaces and thin films, *J. Phys. Chem. B* **110**, 14860 (2006).

[63] N. Seriani, *Ab initio* thermodynamics of lithium oxides: from bulk phases to nanoparticles, *Nanotechnology* **20**, 445703 (2009).

[64] C. Wolverton and K. C. Hass, Phase stability and structure of spinel-based transition aluminas, *Phys. Rev. B* **63**, 024102 (2000).

[65] V. Meng'wa, N. Makau, G. Amolo, S. Scandolo, and N. Seriani, *Ab initio* simulations of copper oxide nanowires and clusters on TiO<sub>2</sub> (101) anatase surface, *J. Phys. Chem. C* **121**, 20359 (2017).

[66] S. K. Iyemperumal, T. G. Fenton, S. L. Gillingham, A. D. Carl, R. L. Grimm, G. Li, and N. A. Deskins, The stability and oxidation of supported atomic-size Cu catalysts in reactive environments, *J. Chem. Phys.* **151**, 054702 (2019).

[67] N. A. Deskins, J. Lauterbach, and K. T. Thomson, Lifting the Pt100 surface reconstruction through oxygen adsorption: A density functional theory analysis, *J. Chem. Phys.* **122**, 184709 (2005).

[68] B. Meyer, Elemental sulfur, *Chem. Rev.* **76**, 367 (1976).

[69] A. J. Jackson, D. Tiana, and A. Walsh, A universal chemical potential for sulfur vapours, *Chemical Science* **7**, 1082 (2016).

[70] K. Yee, R. Barrow, and A. Rogstad, Resonance fluorescence and raman spectra of gaseous sulphur, *J. Chem. Soc., Faraday Trans. 2* **68**, 1808 (1972).

[71] NIST, Janaf thermochemical tables, doi: [10.18434/t42s31](https://doi.org/10.18434/t42s31) (2020).

[72] Y. Kumagai, L. A. Burton, A. Walsh, and F. Oba, Electronic structure and defect physics of tin sulfides: SnS, Sn<sub>2</sub>S<sub>3</sub>, and SnS<sub>2</sub>, *Phys. Rev. Appl.* **6**, 014009 (2016).

[73] H. Schweiger, P. Raybaud, G. Kresse, and H. Toulhoat, Shape and edge sites modifications of MoS<sub>2</sub> catalytic nanoparticles induced by working conditions: A theoretical study, *J. Catal.* **207**, 76 (2002).

[74] M. Bernardi, M. Palummo, and J. C. Grossman, Extraordinary sunlight absorption and one nanometer thick photovoltaics using two-dimensional monolayer materials, *Nano Lett.* **13**, 3664 (2013).

[75] M. V. Bollinger, K. W. Jacobsen, and J. K. Nørskov, Atomic and electronic structure of MoS<sub>2</sub> nanoparticles, *Phys. Rev. B* **67**, 085410 (2003).

[76] M. Sun, A. E. Nelson, and J. Adjaye, Adsorption and dissociation of H<sub>2</sub> and H<sub>2</sub>S on MoS<sub>2</sub> and nimos catalysts, *Catalysis Today* **105**, 36 (2005).